The Journal of the Acoustical Society of America

JANUARY 19 2024

The compression-only behavior of coated microbubbles in a wall restricted flow

Maria Vlachomitrou ; Nikos Pelekasis

J. Acoust. Soc. Am. 155, 452–464 (2024)
https://doi.org/10.1121/10.0024007

ASA
ACOUSTICAL SOCIETY OF AMERICA

JASA ARTICLE

The compression-only behavior of coated microbubbles in a wall restricted flow

Maria Vlachomitrou and Nikos Pelekasis[a)]
Department of Mechanical Engineering, University of Thessaly, Leoforos Athinon, Pedion Areos, 38334 Volos, Greece

ABSTRACT:
The impact that the onset of the compression-only behavior of lipid shelled contrast agents bears on their dynamic interaction with a rigid wall under acoustic disturbances is investigated numerically in the context of axisymmetry. Wall presence is seen to not significantly affect the onset of compression-only since it only reduces the time frame required to trigger the effect. The standoff distance from the wall bears no significant effect on the amplitude threshold except that as it is reduced, it favors asymmetry by altering the compressed buckled shape around which the bubble oscillates. Above the amplitude threshold for parametric shape mode excitation, the onset of compression-only in the vicinity of a rigid wall typically interrupts the process of entrapment by reversing the direction of motion via the positive pressure drug that is generated as a result of the emerging concave upwards buckled shapes. Below this amplitude threshold, symmetric shapes or asymmetric shapes that are concave downwards continue to translate towards the wall where they perform saturated trapped pulsations around nearly spherical flattened or concave downwards buckled shapes. The latter shapes perform compression-only type pulsations and arise on the longer time scale required for the destabilization of the nearly spherical initially trapped shapes. Phase diagrams are constructed identifying regions of trapped pulsations, compression-only response, and microbubble collapse, in the parameter space defined by sound amplitude and shell viscoelastic properties.
https://doi.org/10.1121/10.0024007
(Received 24 March 2023; revised 29 November 2023; accepted 5 December 2023; published online 19 January 2024)
[Editor: Charles C. Church] Pages: 452–464

I. INTRODUCTION

Contrast agents are gas-filled encapsulated microbubbles with their shells usually consisting of a lipid monolayer or a polymeric material. Lipid shells exhibit a strain-softening behavior when subjected to acoustic disturbances (Tsiglifis and Pelekasis, 2008; Thomas *et al.*, 2009; Katiyar and Sarkar, 2011) as their area density decreases with increasing interfacial area. This reduces the effective elasticity of the protective shell thus favoring expansion (Tsiglifis and Pelekasis, 2008; De Jong *et al.*, 2007), especially at large sound amplitudes. However, experimental studies (De Jong *et al.*, 2007; Marmottant *et al.*, 2005) have reported microbubble oscillations with the compression phase being much more intense than the expansion phase, contrary to their strain-softening nature. At certain extreme cases, the bubble is seen to pulsate at a state of compression with respect to its rest radius throughout the periodic cycle, thus bypassing the expansion phase. This behavior is known in the literature as the compression-only behavior and tends to compromise the robustness of acoustic characterization of shell viscoelastic properties.

To capture this dynamic pattern, researchers introduced relatively complex shell models since pre-existing models that accounted for shell elasticity failed to reproduce experimental observations. Marmottant *et al.* (2005) introduced an effective surface tension that depends highly on the surface concentration of phospholipid molecules. According to their model, surface tension varies from zero when the bubble is highly compressed, in which case the shell is treated as a buckled shell, to the value of the air-water system when the bubble expands above a critical limit where shell rupture is assumed. Between these two limits, an elastic state is considered where surface tension depends linearly on the area of the shell. By considering an initially compressed state of the bubble due to the dissolution of a certain amount of gas in the surrounding liquid and by taking the initial radius of the bubble to be the critical limit below which a solid state is entered, they captured compression-only behavior. This approach, which has been used in other studies as well (Sarkar *et al.*, 2005; Paul *et al.*, 2010), neglects the bending modulus and fails to capture the onset of buckling at a certain finite compression in the manner indicated by experiments (Overlede, 2009). In a different approach, Doinikov *et al.* (2009) included non-linear effects in the variation of shell viscosity by allowing for shear-thinning behavior of the shell. Thus, they numerically capture compression-only behavior as reported by de Jong *et al.* (2007), but do not recover the resonance frequencies of coated microbubbles based on acoustic measurements.

In a more recent study, Pelekasis *et al.* (2022), hereinafter referred to as **I** for brevity, captured compression-only behavior for lipid shells by assuming constant rheological shell properties, introducing the area dilatation and bending stiffness as well as a discrepancy between shear and dilatational shell viscosities. Moreover, they adopted the

[a)]Email: pel@uth.gr

https://doi.org/10.1121/10.0024007

assumption of an initially pre-stressed compressed shell due to gas leakage. They conducted a theoretical/numerical study and demonstrated that this behavior is associated with the onset of significantly compressed buckled shapes that pulsate in the vicinity of static branches bifurcating from the spherosymmetric configuration. They showed that an initially pre-stressed state generates a window of sound amplitudes between the static buckling and the dynamic buckling thresholds, within which parametric excitation of shape modes that correspond to the statically bifurcating branches is possible. In this case, and especially when the discrepancy between the two shell viscosities is large, the dynamics leads towards pulsation around compressed buckled shapes.

In a former study, Vlachomitrou and Pelekasis (2021a,b) studied the dynamic response of an initially stress-free contrast agent that is subject to acoustic disturbances and identified the mechanism and relevant conditions that govern the trapping process in the vicinity of a rigid wall when the two shell viscosities are equal. It was thus found that when the sound amplitude remains smaller than a critical value, identified as the dynamic buckling threshold beyond which explosive shape mode excitation and shell breakup take place (Tsiglifis and Pelekasis, 2011), the microbubble is eventually trapped at a small distance from the wall where it performs steady pulsations. In the present study, we wish to investigate the extent to which compression-only behavior affects the dynamic response of contrast agents subject to acoustic disturbances in a wall bounded flow, with emphasis on trapping by the wall. To this end, we adopt the model considered in **I** and investigate whether the proposed mechanism is affected by the proximity of the boundary and the extent to which the trapping process is affected by the onset of the compression-only behavior, as this is modified by wall presence.

In the context of coated microbubbles, migration and trapping may play a central role in the microstreaming effect and the potential for novel drug delivery modalities (Marmottant and Hilgenfeldt, 2003). We should also point out that previous experimental studies with conventional bubbles pulsating near compliant surfaces (Shima *et al.*, 1989) stress the impact of standoff distance, wall stiffness, and inertia on bubble migration with respect to the wall and the potential for prevention of damage. In the present study, we focus on the combined effect of standoff distance and shell viscoelastic properties on microbubble migration while leaving the effect of wall elasticity to a future study.

The paper is organized as follows: the problem formulation is discussed in Sec. II, where the governing equations for the liquid flow are presented along with the ones describing the encapsulated bubble. Next, in Sec. III, the numerical methodology is briefly described as it has been presented in detail by Vlachomitrou and Pelekasis (2021a). Subsequently, in Sec. IV the results of the dynamic simulations are presented and discussed while in Sec. V the main conclusions of the study are summarized.

II. PROBLEM FORMULATION

We wish to extend the study presented in **I** to take into account wall presence. In this fashion, we study the response of an encapsulated microbubble of initial radius R_0 to an acoustic disturbance imposed on the far field,

$$P_\infty = P_{st} + P_{dist} = P_{st} + P_{st}\varepsilon\cos(t), \tag{1}$$

where P_{st}, P_{dist} denote the dimensionless undisturbed and disturbed pressure in the far field, respectively, and ε the amplitude of the acoustic disturbance. The imposed disturbance represents a standing wave with negligible spatial modulation indicating a pressure wave with a much larger wavelength with respect to the bubble radius and standoff distance. Therefore, the acoustic field does not induce a primary Bjerknes force on the microbubble. Rather it triggers volume pulsations and a translational motion of the bubble due to the secondary Bjerknes force resulting from wall interaction (Vlachomitrou and Pelekasis, 2021a). The undisturbed pressure in the far field is fixed to the standard atmospheric pressure, 101.325 kPa. The microbubble is submerged in a Newtonian liquid of density ρ and dynamic viscosity μ that is bounded by a rigid wall. The initial radius R_0 of the bubble is taken as the characteristic length scale, whereas the external frequency sets the appropriate time scale to $1/\omega_f$, with ω_f being the forcing frequency of the pressure disturbance. In this context, the characteristic velocity and pressure scales are equal to $\omega_f R_0$ and $\rho\omega_f^2 R_0^2$, respectively. We allow the microbubble to be initially in a pre-stressed state since it was found to be of critical importance for the onset of the compression-only behavior,

$$R_0 = R_{SF} + U_d, \tag{2}$$

where R_{SF} is the radius of the stress-free spherical bubble and $U_d < 0$ signifies the amount of initial radial compression imposed on the stress-free radius.

In order to obtain the governing equations, we employ the cylindrical coordinate system, and we assume axisymmetric variations of the bubble shape as well as the liquid velocity and pressure. A schematic representation of the flow under consideration is provided in Fig. 1 with f_1 denoting the r-coordinate of the thin shell that coats the bubble.

For the incompressible liquid that surrounds the microbubble, the mass conservation and momentum equations expressed through the continuity and Navier-Stokes equations read in dimensionless form,

$$\nabla\cdot\boldsymbol{u} = 0, \tag{3}$$

$$\frac{\partial \boldsymbol{u}}{\partial t} + (\boldsymbol{u}\cdot\nabla)\boldsymbol{u} = -\nabla P + \frac{1}{\mathrm{Re}}\nabla\cdot\underline{\underline{\tau_l}},$$

$$\underline{\underline{\sigma}} = -P\underline{\underline{I}} + \frac{1}{\mathrm{Re}}\underline{\underline{\tau_l}}, \quad \underline{\underline{\tau_l}} = \nabla\boldsymbol{u} + \nabla\boldsymbol{u}^T, \tag{4}$$

where $\mathbf{u} = (u_r, u_z, 0)$, $\mathrm{Re} = (\rho\omega_f {R_0}^2)/\mu$ is the Reynolds number of the flow that compares inertia with viscous

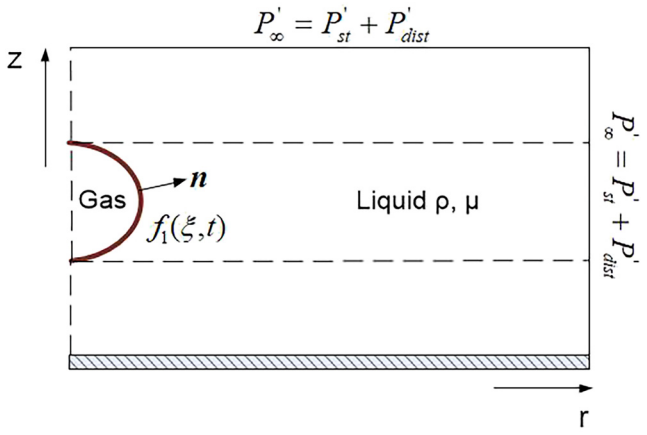

FIG. 1. (Color online) A contrast agent in a wall restricted flow.

forces, $\underline{\underline{\boldsymbol{\sigma}}}$, $\underline{\underline{\boldsymbol{\tau}}}_l$, the full and deviatoric stress tensors in the surrounding fluid, and $\underline{\underline{\boldsymbol{I}}}$ the unit tensor.

The interface is described via the Lagrangian coordinate ξ $(0 \le \xi \le 1)$ with $\xi = 0$ and $\xi = 1$ corresponding to the south and north poles of the bubble, respectively. On the gas-liquid interface the force balance is given by

$$\left(-P\underline{\underline{\boldsymbol{I}}} + \frac{1}{\mathrm{Re}}\underline{\underline{\boldsymbol{\tau}}}_l\right)\cdot\boldsymbol{n} + P_G\boldsymbol{n} = -\nabla_s\cdot\left(\underline{\underline{\tau}} + \boldsymbol{q}\boldsymbol{n}\right) + \frac{2k_m}{We}\boldsymbol{n} = \boldsymbol{\Delta F} + \frac{2k_m}{We}\boldsymbol{n}, \tag{5}$$

where $\boldsymbol{n} = \left(z_\xi/\sqrt{r_\xi^2 + z_\xi^2}\right)\boldsymbol{e_r} - \left(r_\xi/\sqrt{r_\xi^2 + z_\xi^2}\right)\boldsymbol{e_z}$ is the unit normal vector pointing towards the surrounding fluid, P_G the gas pressure inside the bubble, ∇_s,k_m the surface gradient and mean curvature of the bubble interface, respectively, $\boldsymbol{q}$ the transverse shear force resultant and $We = \rho\omega_f^2 {R_0}^3/\sigma$ is the Weber number comparing inertia with capillary forces. Following previous studies for lipid shells (Marmottant *et al.*, 2005; Sarkar *et al.*, 2005; Church, 1995; Khismatullin and Nadim, 2002) we assume a certain amount of surface tension, $\sigma = 0.051$ N/m, as a measure of the internal gas exposure to the surrounding liquid. Finally, $\boldsymbol{\Delta F}$ is the resultant force due to the viscoelastic properties of the membrane,

$$\boldsymbol{\Delta F} = \left[k_s\tau_s + k_\phi\tau_\phi - \frac{1}{r}\frac{\partial}{\partial s}(rq)\right]\boldsymbol{n} - \left[\frac{\partial\tau_s}{\partial s} + \frac{1}{r}\frac{\partial r}{\partial s}(\tau_s - \tau_\phi) + k_s q\right]\boldsymbol{e}, \tag{6}$$

with s, ϕ denoting the interfacial arc length and azimuthal directions, respectively, τ_s, τ_ϕ the principal stress resultants, k_s, k_ϕ the two principal curvatures, r the cylindrical polar coordinate, and $\boldsymbol{e}_s$ the tangential unit vector. In Eq. (6), q expresses the transverse shear tension that is obtained from a torque balance on the shell (Timoshenko and Woinowsky-Krieger, 1959; Pozrikidis, 2001),

$$q = \frac{K_B}{r}\frac{\partial r}{\partial s}\left[\frac{\partial}{\partial r}(rm_s) - m_\phi\right], \quad K_B = \frac{k_B}{\rho\omega_f^2 R_0^5}, \tag{7}$$

with m_s, m_ϕ being the principal bending moments, k_B the bending modulus, and K_B signifying the relative importance of bending with respect to inertia. The principal membrane tensions consist of an elastic, τ_{el}, and a viscous component, τ_v,

$$\tau_s = \tau_{s,el} + \tau_{s,v}\ ; \quad \tau_\phi = \tau_{\phi,el} + \tau_{\phi,v}. \tag{8}$$

For the elastic part, since we consider lipid shells, we adopt the Mooney Rivlin (MR) constitutive law (Barthes-Biesel *et al.*, 2002) with the degree of softness b set to zero (Barthes-Biesel *et al.*, 2002; Tsiglifis and Pelekasis, 2008),

$$\tau_{s,el}^{MR} = \frac{G}{3\lambda_s\lambda_\varphi}\left(\lambda_s^2 - \frac{1}{(\lambda_s\lambda_\varphi)^2}\right)\left[1 + b\left(\lambda_\varphi^2 - 1\right)\right], \tag{9a}$$

$$\tau_{\phi,el}^{MR} = \frac{G}{3\lambda_s\lambda_\varphi}\left(\lambda_\phi^2 - \frac{1}{(\lambda_s\lambda_\varphi)^2}\right)\left[1 + b\left(\lambda_s^2 - 1\right)\right], \tag{9b}$$

where $G = \chi/(\rho\omega_f^2 R_0^3)$ signifies the relative importance of shell dilatation with respect to inertia and λ_s, λ_φ correspond to the principal extension ratios based on the stress-free state,

$$\lambda_s = \frac{s_\xi(t)}{s_\xi(0)}, \quad \lambda_\phi = \frac{r(t)}{r(0)}, \quad s_\xi = \sqrt{r_\xi^2 + z_\xi^2}. \tag{10}$$

For the viscous part, the dilatational viscosity μ_s and the shear viscosity μ_{sh} of the shell are treated separately. More specifically, the viscous components of the membrane tensions read as

$$\tau_s^v = \left(\frac{1}{\mathrm{Re}_s} + \frac{1}{\mathrm{Re}_{sh}}\right)\frac{1}{\lambda_s}\frac{\partial\lambda_s}{\partial t} + \left(\frac{1}{\mathrm{Re}_s} - \frac{1}{\mathrm{Re}_{sh}}\right)\frac{1}{\lambda_\varphi}\frac{\partial\lambda_\varphi}{\partial t}, \tag{11a}$$

$$\tau_\phi^v = \left(\frac{1}{\mathrm{Re}_s} + \frac{1}{\mathrm{Re}_{sh}}\right)\frac{1}{\lambda_\phi}\frac{\partial\lambda_\phi}{\partial t} + \left(\frac{1}{\mathrm{Re}_s} - \frac{1}{\mathrm{Re}_{sh}}\right)\frac{1}{\lambda_s}\frac{\partial\lambda_s}{\partial t}, \tag{11b}$$

with $\mathrm{Re}_s = \rho\omega_f R_0^3/\mu_s$ and $\mathrm{Re}_{sh} = \rho\omega_f R_0^3/\mu_{sh}$ comparing inertia forces with the viscous dilatational and shear forces of the shell, respectively.

The continuity of the liquid and shell velocities is, also, applied on the interface,

$$\boldsymbol{u} = \frac{D\boldsymbol{r_s}}{Dt}, \tag{12}$$

with $\boldsymbol{r_s} = r\boldsymbol{e}_r + z\boldsymbol{e}_z$ corresponding to the position vector of a particle at the interface. Initially, the microbubble is taken to be spherical, surrounded by a fluid at static equilibrium. The initial axial position of the center of volume of the bubble with respect to the wall, z_{c0}, is the standoff distance and its impact on the dynamics will be investigated in the following. The dimensionless pressure, P_G, inside the bubble at static equilibrium is related to the dimensionless pressure, P_{st}, in the far field as follows:

$$P_G(t=0) = P_{st} + \frac{2}{We} + 2\tau_{el}(t=0). \tag{13}$$

https://doi.org/10.1121/10.0024007

The extra elastic term in the previous equation corresponds to the initial stress state of the shell due to the external overpressure that arises as a result of gradual gas leakage through the shell before the application of the acoustic disturbance. By assuming uniform gas pressure inside the bubble due to negligible density and kinematic viscosity and the fact that heat transfer between the bubble and the surrounding liquid occurs extremely fast compared to the time scale of the problem, bubble oscillations are characterized as nearly isothermal, and the bubble pressure is given by

$$P_G(t=0)V_G^{\gamma}(t=0) = P_G(t)V_G^{\gamma}(t) = const., \tag{14}$$

with V_G denoting the dimensionless instantaneous volume of the bubble, $V_G(t=0) = 4\pi/3$ the initial volume of the bubble, and γ the polytropic constant set to 1.07. The latter value is also close to the ratio of specific heats of certain ideal gases that are carried by known contrast agents and undergo adiabatic pulsations during insonation (Tsiglifis and Pelekasis, 2008; Marmottant *et al.*, 2005; Sarkar *et al.*, 2005; Vlachomitrou and Pelekasis, 2021a,b).

III. NUMERICAL METHODOLOGY

The numerical method employed in this study as well as the code validation with appropriate benchmark tests have been presented in detail in Vlachomitrou and Pelekasis (2021a). In the latter study, the dilatational and shear shell viscosities were treated as equal and the microbubble as initially stress-free, whereas in the present study, the two viscosities are taken as different parameters while allowing for an initially pre-stressed state as in **I** where an unbounded flow is considered. However, these extra considerations in the problem formulation do not affect the numerical methodology. Therefore, following the study that concerns a wall restricted flow, the numerical solution is performed via the Galerkin Finite Element Methodology by employing biquadratic and bi-linear Lagrangian basis functions to discretize the velocity and the pressure of the liquid, respectively, in conjunction with one-dimensional (1D) cubic splines for the bubble interface. Time integration is implemented via the fully implicit Euler scheme, whereas the non-linearity of the problem is treated with the Newton-Raphson method. The final set of the linearized equations is solved iteratively with the Generalized Minimal Residual (GMRES) method.

As an overall numerical procedure, at each time step two separate Newton-Raphson procedures are applied. In the first procedure, the governing equations presented in Sec. II are solved simultaneously to obtain the velocity and pressure fields along with the shape of the interface. A second Newton-Raphson iterative procedure follows, in order to implement the elliptic mesh generation technique and to adjust the grid to the interfacial shape, which is already known from the first procedure and is imposed as an essential condition. According to the elliptic technique, every point (r,z) of the physical domain in a particular time instant is mapped onto a grid point with coordinates (η,ξ): $(\mathrm{r},\mathrm{z},\mathrm{t}) \rightarrow (\eta,\xi,\mathrm{t})$. The coordinates of the grid points in the physical domain are obtained by solving the following set of partial differential equations (Tsiveriotis and Brown, 1992; Dimakopoulos and Tsamopoulos, 2003),

$$\nabla\cdot\left[\left(\varepsilon_1\sqrt{\frac{r_\xi^2+z_\xi^2}{r_\eta^2+z_\eta^2}}+1-\varepsilon_1\right)\nabla\xi\right]=0, \tag{15}$$

$$\nabla\cdot\nabla\eta=0, \tag{16}$$

where $r_\xi, r_\eta, z_\xi, z_\eta$ are the partial derivatives of the physical coordinates r, z with respect to the computational coordinates ξ, η. The previous equations are discretized using the biquadratic Lagrangian basis functions. The first equation generates the η-curves of the computational domain that intersect the interface almost orthogonally, whereas the second equation produces the ξ-curves, which are nearly parallel to the interface. In the first equation, ε_1 is an empirical parameter defined by trial and error that controls the extent of mesh smoothness versus its orthogonality. This parameter ranges between 0 and 1 and in our case is set to 0.1. As far as the boundary conditions are concerned, in any boundary where one of the coordinates is known, the distribution of corresponding values is imposed as an essential boundary condition. When it is unknown, the integral terms that the divergence theorem produces in the discretized form of the grid equations are omitted to weakly impose the orthogonality of the grid lines in these boundaries. The discretized form of the governing equations, details about the implementation of the Newton-Raphson and the GMRES methods, as well as details on the implementation of the elliptic mesh generation technique can be found in Vlachomitrou and Pelekasis (2021a).

IV. RESULTS AND DISCUSSION

We consider a lipid shelled contrast agent that is characterized by an area dilatational modulus $\chi = 0.24$ N/m, bending modulus $k_B = 3\times10^{-14}$Nm, shell thickness $\delta = 1$ nm, and shear shell viscosity $\mu_{sh} = 60\times10^{-9}$kg/s. The microbubble has a stress-free radius $R_{SF} = 3.6\,\mu$m and due to gas leakage is at an initially compressed state with $U_d = -0.46\,\mu$m. Thus, the initial radius of the bubble, $R_0 = 3.14\mu$m, is slightly above the critical threshold for static buckling since it corresponds to a radial compression of $R_0/R_{SF} \approx 0.872$ when the critical compression for buckling to occur is $R_B/R_{SF} \approx 0.87$, pertaining to a bifurcating branch emerging at a critical amplitude $\varepsilon_{cr} \approx 0.04$ (Pelekasis *et al.*, 2022). In this way, we ensure that, in the absence of geometric imperfections, any shape deformations will only be excited acoustically. In **I**, the phase diagram for the previously mentioned parameters was constructed in the absence of an interacting wall, as a function of the ratio of shear to dilatational viscosity of the shell, μ_{sh}/μ_s, both in the presence and in the absence of initial prestress when the external acoustic frequency was set to $f = 1.7$ MHz [see Figs. 2(a) and 2(b)]. The phase diagrams were obtained by performing Floquet type stability analysis on the spherosymmetric pulsations of an acoustically excited

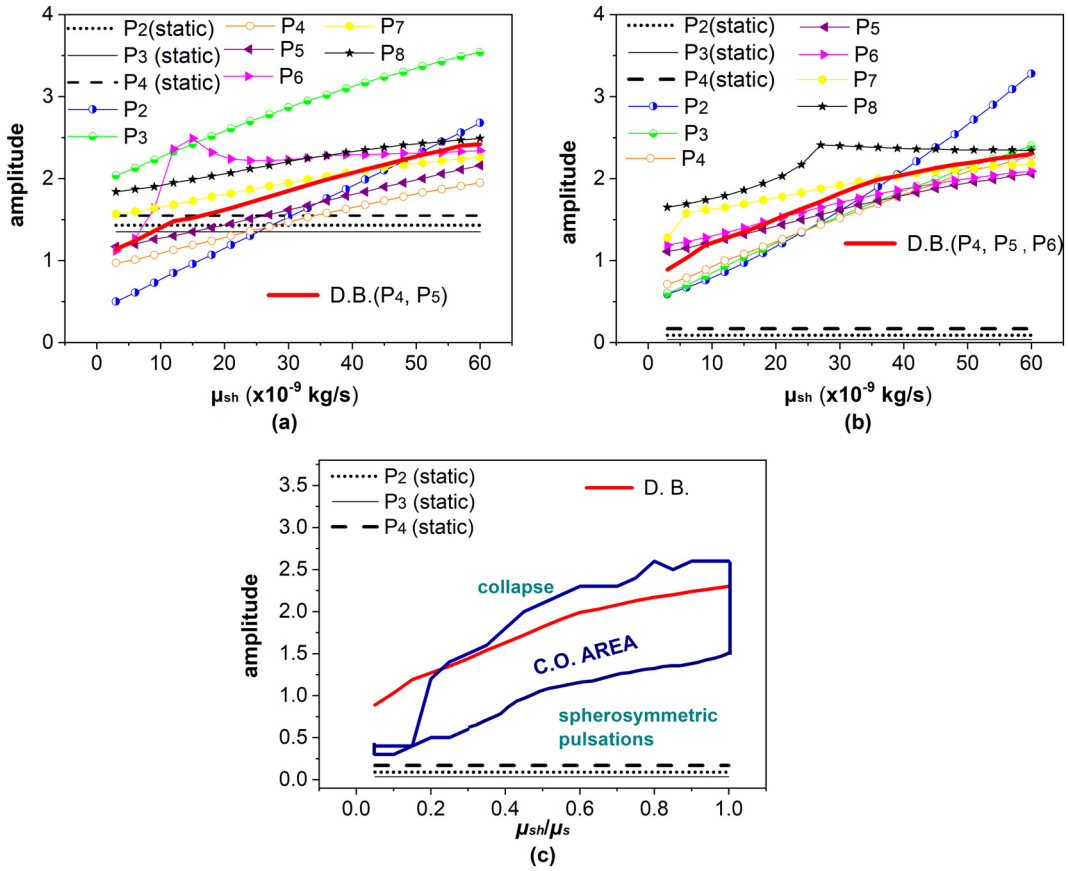

FIG. 2. (Color online) Phase diagram with increasing μ_{sh}/μ_s ratio for a lipid coated microbubble ($R_{SF} = 3.6\,\mu$m, $\mu_s = 60 \times 10^{-9}$ kg/s, $\chi = 0.24$ N/m, $k_B = 3 \times 10^{-14}$ N·m, $\delta = 1$ nm) subject to (a) no initial prestress, (b and c) an initial prestress of $U_d = -0.46\,\mu$m, and an acoustic disturbance of $f = 1.7$ MHz; (c) includes the region where compression-only (C.O area) is exhibited in the absence of a wall, according to **I**.

contrast agent allowing for small axisymmetric disturbances in an inviscid and unbounded flow and were complemented by simulations. The analysis followed the study by Tsiglifis and Pelekasis (2011) with the exception of shell viscosity that consisted of shear and dilatational components with a varying degree of disparity, as opposed to being set as equal in the latter study.

In this context, the lines P_n throughout Fig. 2 illustrate the amplitude thresholds for the parametric excitation of the *n*th Legendre mode within a time interval of 30 periods of the forcing and for the dynamic buckling to occur. Dynamic buckling (D.B.) refers to a Rayleigh-Taylor type instability that occurs very fast (within ten periods of the forcing) during the rebound phase that follows maximum volume compression with the rapid growth of many shape modes that leads to loss of shell cohesion and breakup of the microbubble (Tsiglifis and Pelekasis, 2011). Upon close inspection of Fig. 2(a), it is clear that varying the discrepancy between shear and dilatational shell viscosity for a vanishing amount of prestress merely reduces the threshold for parametric mode excitation and dynamic buckling to occur. In the same context, the static buckling thresholds in the absence of prestress have been added as horizontal lines since they do not depend on shell viscosity. Each horizontal line corresponds to the critical threshold for a different bifurcating branch from the main spherosymmetric solution family that is dominated by the nth Legendre mode. The complete bifurcation diagram for this case is also given in **I**.

When an initial amount of prestress is present the phase diagram is shown in Fig. 2(b). Numerical simulations performed in **I** in the absence of a nearby wall revealed that the compression-only behavior is possible, within a window in the sound amplitude that is established above the amplitude threshold for static growth of shape modes. More specifically, it occupies the amplitude interval above the threshold for parametric excitation of the shape mode that characterizes a certain bifurcating branch and below the onset of dynamic buckling, both identified in Fig. 2(b). In particular, it was seen that this behavior is associated with the onset of significantly compressed buckled shapes that pulsate in the vicinity of the static non-spherical branches. It was also verified by numerical simulations, that shells with a small shear viscosity compared to the dilatational one facilitate the transfer of energy from volume pulsation to shape modes thus providing a distinctly lower amplitude threshold, in comparison with higher modes, for parametric excitation of shape modes that correspond to the statically bifurcating branches.

Figure 2(c) presents a complete parametric study, based on numerical simulations, that complements the phase diagram provided in Fig. 2(b) by providing the domain in phase

https://doi.org/10.1121/10.0024007

space for which compression-only behavior is captured numerically, it is marked as C.O. area, in the absence of a nearby wall. Clearly, the latter region in parameter space correlates well with the window defined by the two previously-mentioned amplitude thresholds for parametric instability and dynamic buckling. Such a response pattern could not be recovered in the absence of prestress, Fig. 2(a), due to the increased buckling amplitude threshold that approaches the parametric and dynamic buckling thresholds. In Fig. 2(c), the term "collapse" is used to describe either the collapse of the bubble via dynamic buckling or via direct contact between the two poles in the manner presented in **I**. Below the lower limit of the C.O. area, no excitation of shape modes occurs and, thus, the bubble keeps performing spherosymmetric pulsations.

The same type of coated microbubble was employed by Vlachomitrou and Pelekasis (2021a,b) in their numerical study of trapped pulsations near a rigid wall, in the absence of initial prestress for identical shear and dilatational shell viscosities. It was found that wall presence suppresses excessive growth of the dominant shape modes predicted by parametric excitation stability analysis, by triggering the onset of a large number of asymmetric modes. In this fashion, trapped pulsations were captured at a small distance from the wall, on the order of a few tenths of nm. During this state, the bubble performs saturated volume pulsations, with its shape varying between an almost spherical shape at maximum expansion and an oblate shape with a flattened shell portion near the pole that faces the wall at maximum compression, e.g., see Figs. 3 and 5 from Vlachomitrou and Pelekasis (2021b) and panels in Fig. 7 from the present study. For sound amplitudes close to the prediction for dynamic buckling to occur, rapid growth of shape modes was evident leading to loss of coherence of the shell and breakup.

In the present study, it is of interest to explore the manner in which the compression-only mechanism identified in **I** is affected by wall presence and, moreover, to determine whether and how this effect impacts the trapping procedure studied by Vlachomitrou and Pelekasis (2021a,b). As in **I**, we consider that the "compression-only" behavior is triggered in time as soon as we capture oscillations where the amplitude of compression below the equilibrium radius is much greater than the amplitude of expansion above it.

In this context, in Figs. 3 and 4 we contrast the numerical simulations for a wall restricted and an unbounded flow

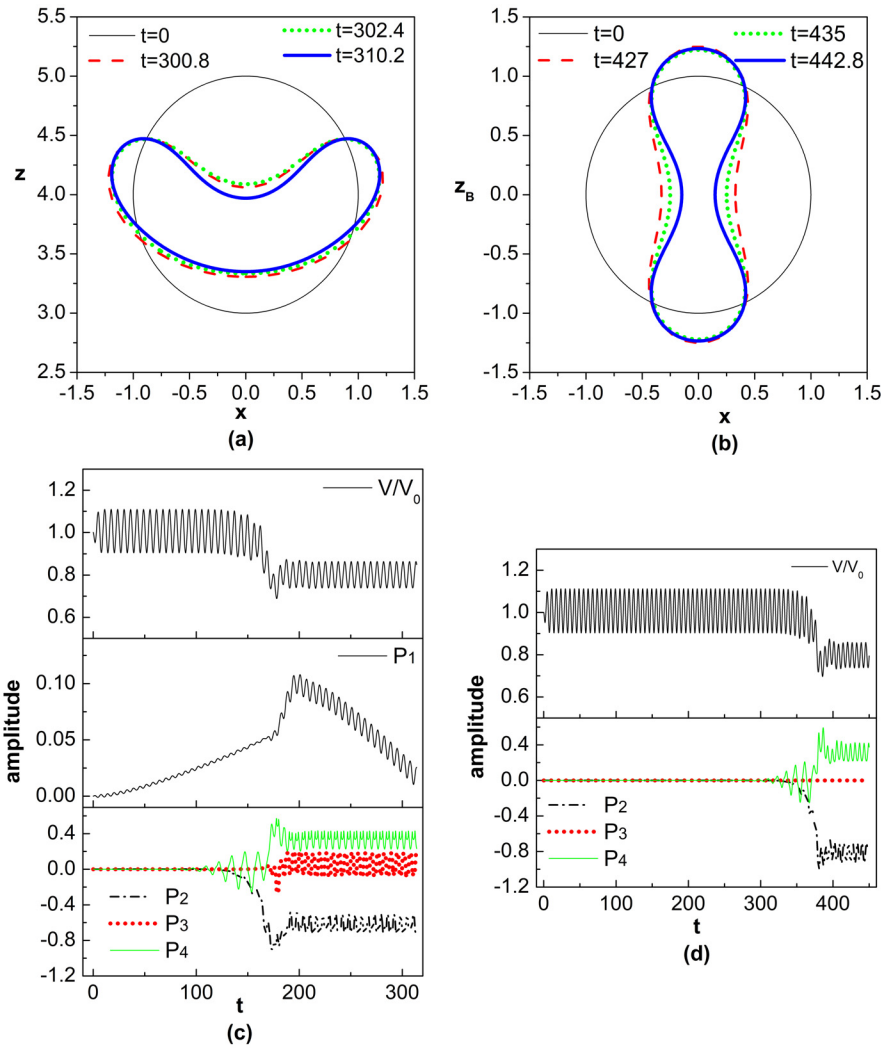

FIG. 3. (Color online) Temporal evolution of (a) and (b) bubble shape and (c) and (d) the volume and shape mode pulsation, for a lipid coated microbubble ($R_{SF}=3.6\,\mu$m, $\mu_s=60\times10^{-9}$ kg/s, $\chi=0.24$ N/m, $k_B=3\times10^{-14}$ N m, $\delta=1$ nm) subject to an acoustic disturbance with $f=1.7$ MHz and $\varepsilon=0.3$ for an initial prestress, $U_d=-0.46\,\mu$m and $\mu_{sh}/\mu_s=0.1$ for (a) and (c) a wall restricted flow when the initial distance from the wall is set to $z_{c0}=4$ and (b) and (d) an unbounded flow.

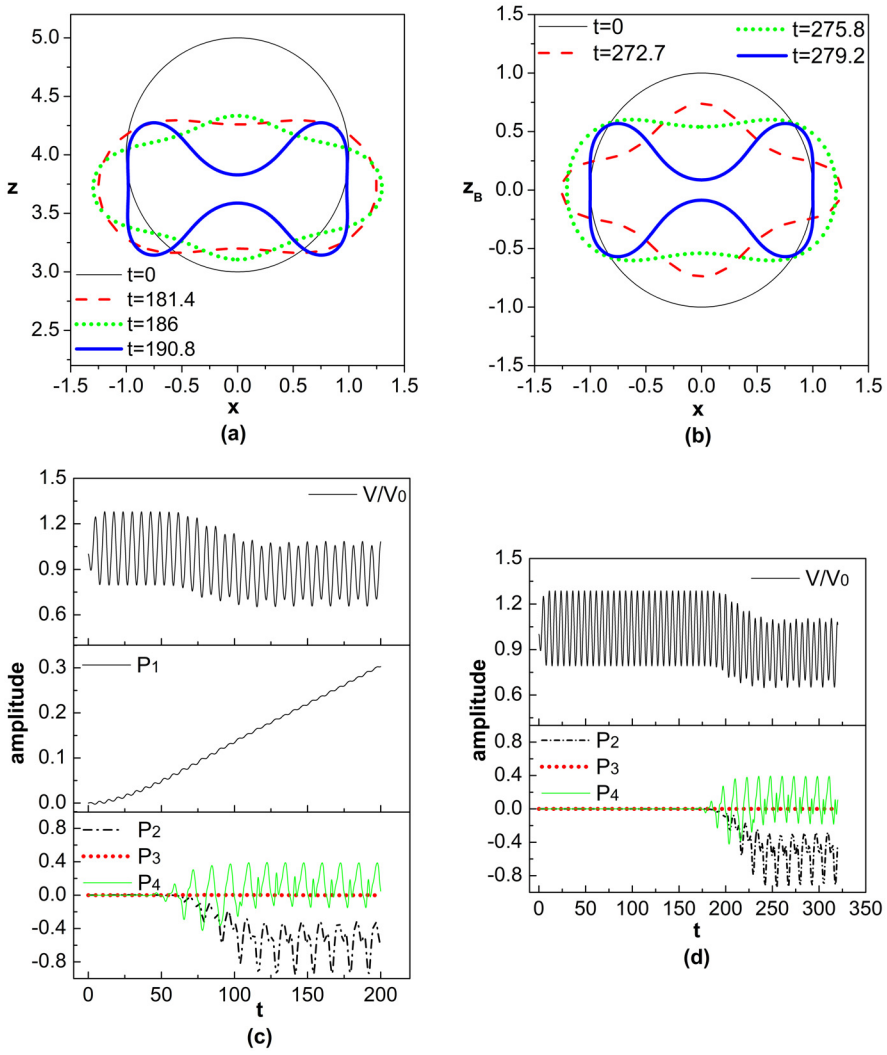

FIG. 4. (Color online) Temporal evolution of (a) and (b) bubble shape and (c) and (d) the volume and shape mode pulsation, for a lipid coated microbubble ($R_{SF} = 3.6\,\mu$m, $\mu_s = 60 \times 10^{-9}$ kg/s, $\chi = 0.24$ N/m, $k_B = 3 \times 10^{-14}$ N m, $\delta = 1$ nm) subject to an acoustic disturbance with f = 1.7 MHz and $\varepsilon = 0.7$ for an initial prestress, $U_d = -0.46\,\mu$m and $\mu_{sh}/\mu_s = 0.3$ for (a) and (c) a wall restricted flow when the initial distance from the wall is set to $z_{c0} = 4$ and (b) and (d) an unbounded flow.

for two different ratios of shear to dilatational shell viscosity, μ_{sh}/μ_s, respectively. In particular, the microbubble depicted in Fig. 3 ($\mu_{sh}/\mu_s = 0.1$) performs oscillations around a symmetric shape when an unbounded flow is considered, Figs. 3(b) and 3(d), whereas the presence of the wall drives the oscillation towards the energetically favored P_3 asymmetric brunch, manifested in the asymmetric shape pulsations captured in Figs. 3(a) and 3(c). However, in both cases, the shape is still dominated by the shape modes P_2, P_3, and P_4 that correspond to the static bifurcating branches, with P_3 clearly emerging as a dominant mode when the wall is present. On the other hand, in the case presented in Fig. 4 ($\mu_{sh}/\mu_s = 0.3$), wall presence does not significantly affect the compressed buckled shape around which the bubble oscillates, and it simply reduces the number of periods needed for the onset of the phenomenon.

Throughout Sec. IV, the interfacial shape in the unbounded flow is illustrated in terms of the Cartesian coordinates $z_B = r_{sph}\cos\theta$ and $x = r_{sph}\sin\theta$ where r_{sph}, θ, φ, signify the spherical radius, the azimuthal angle, and the polar angle, respectively. Typically, the (x, z_B) plane is obtained by joining the $\varphi = 0$ and $\varphi = \pi$ surfaces and, thus, the z_B coordinate is aligned with the axis of symmetry with its origin located at the geometric center of the bubble. Axial coordinate z is used in the graphs illustrating the bubble shape as it interacts with the wall, with its origin lying at the wall and z_{c0} denoting the initial distance of the geometric center of the bubble from the wall, i.e., the standoff distance. In the context of axisymmetry, the interface is symmetric in the (x, z_B) plane with respect to the z_B axis for an unbounded flow, whereas in the (x, z) plane, it is symmetric with respect to the z-axis for a wall restricted flow. In all graphs, time is made dimensionless with the characteristic time scale, $1/\omega_f$, equal to 0.0936μs, whereas the mode amplitude is made dimensionless using the initial bubble radius $R_0 = 3.14\,\mu m$.

An important aspect of microbubble migration in the previous simulations pertains to the reversion of direction exhibited in Fig. 3(c) at the onset of the compression-only behavior, at which point asymmetric buckled shapes emerge as a result of parametric mode excitation. Such a pattern was not obtained in cases for which symmetric shapes are obtained as can be gleaned from Fig. 4. In fact, Fig. 4(c) illustrates the persistence of bubble migration towards the wall, despite the onset of compression-only, as long as the emerging buckled shapes remain symmetric. However, as

https://doi.org/10.1121/10.0024007

will be seen in the following, this pattern will be modified as the bubble translates towards the wall in which case asymmetric shapes will arise.

In order to assess the effect of wall distance a series of simulations is performed with decreasing standoff distance starting from the case portrayed in Figs. 4(a) and 4(c). It is thus seen, as illustrated in Figs. 5 and 6, that wall proximity does not significantly affect the amplitude threshold for the onset of compression-only since it is associated with the onset of parametric shape mode excitation. However, reducing the standoff distance reduces the time scale required for this dynamic response pattern to emerge, provided the amplitude threshold is exceeded while favoring the growth of asymmetric, pulsating buckled shapes. This becomes evident upon comparing Figs. 4(a) and 4(c), with Figs. 6(a) and 6(b) and 5(b) and 5(d), which correspond to the same parameter range but to a gradually decreasing initial distance from the wall. In fact, in cases where parametric mode excitation favors the growth of symmetric shape modes in the early stages of the phenomenon, in the manner depicted in Figs. 4, 5, and 6, as the distance from the wall is reduced, due to bubble migration towards the wall, asymmetric modes prevail and the shape around which the bubble oscillates becomes asymmetric, Figs. 5(b) and 6(a). This effect is not captured in Figs. 4(b) and 4(d) due to the large initial distance and the resulting slow evolution of the dynamics, but it is expected to arise at a later stage of the simulation as clearly illustrated in Fig. 6(b) where, despite the reduced initial distance ($z_{c0} = 2.5$ instead of 2), the symmetric modes P_2 and P_4 still emerge first. In this context, we clearly capture transition from the type of symmetric buckled shape shown in Fig. 4 to the asymmetric shape of Fig. 5(b), see the shapes and shape mode evolution captured in Fig. 6. However, as the standoff distance approaches the wall the asymmetric P_3 mode starts growing first and becomes dominant, leading to the asymmetric shapes shown in Fig. 5. Therefore, as an overall pattern, reduction of the stand-off distance does not bear a significant impact on the amplitude threshold but rather accelerates the onset of asymmetric modes.

As was already pointed out previously, a very important aspect of the response of contrast agents to acoustic

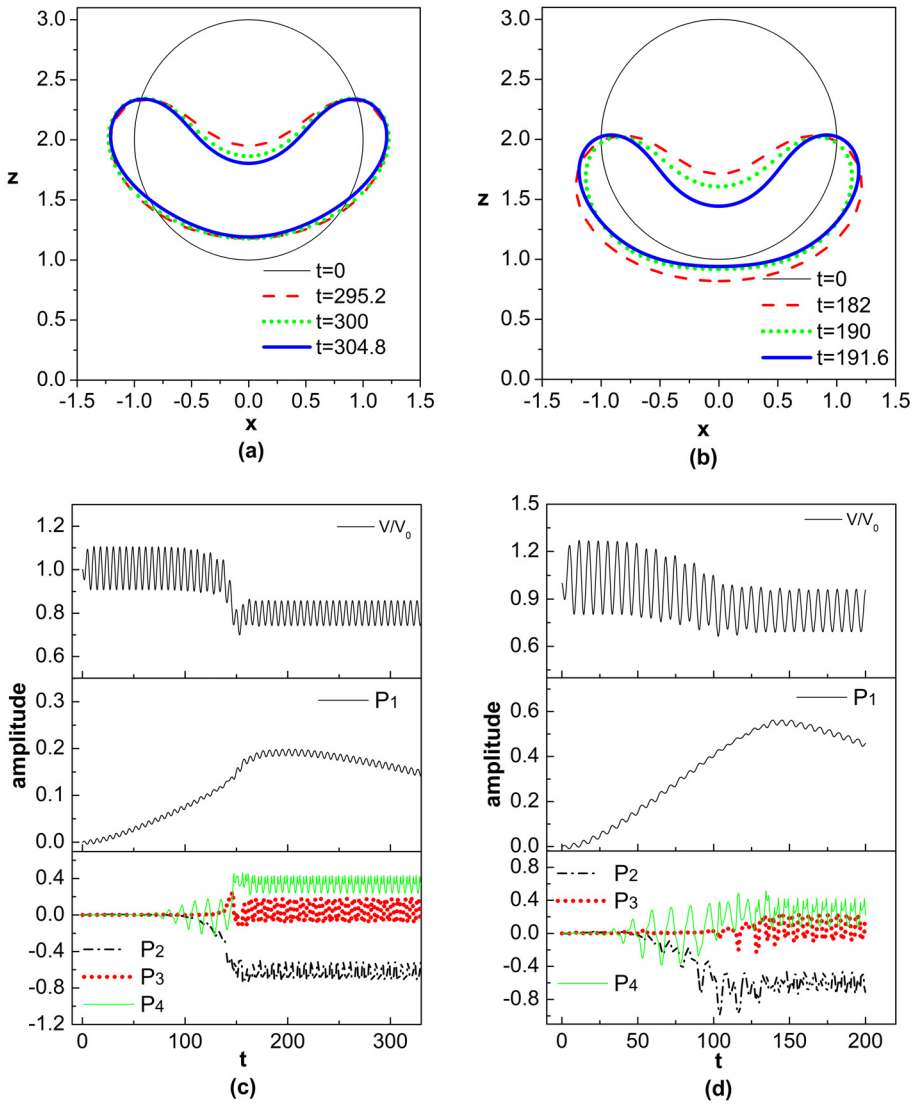

FIG. 5. (Color online) Temporal evolution of (a) and (b) bubble shape and (c) and (d) the volume, the translational mode P_1 and shape mode pulsation, for a lipid coated microbubble ($R_{SF} = 3.6\,\mu$m, $\mu_s = 60 \times 10^{-9}$ kg/s, $\chi = 0.24$ N/m, $k_B = 3 \times 10^{-14}$ N m, $\delta = 1$ nm) subject to an acoustic disturbance with f = 1.7 MHz and an initial prestress, $U_d = -0.46\,\mu$m when, (a) and (c) $\mu_{sh}/\mu_s = 0.1$ and $\varepsilon = 0.3$ and (b) and (d) $\mu_{sh}/\mu_s = 0.3$ and $\varepsilon = 0.7$, for a wall restricted flow with the initial distance from the wall set to $z_{c0} = 2$.

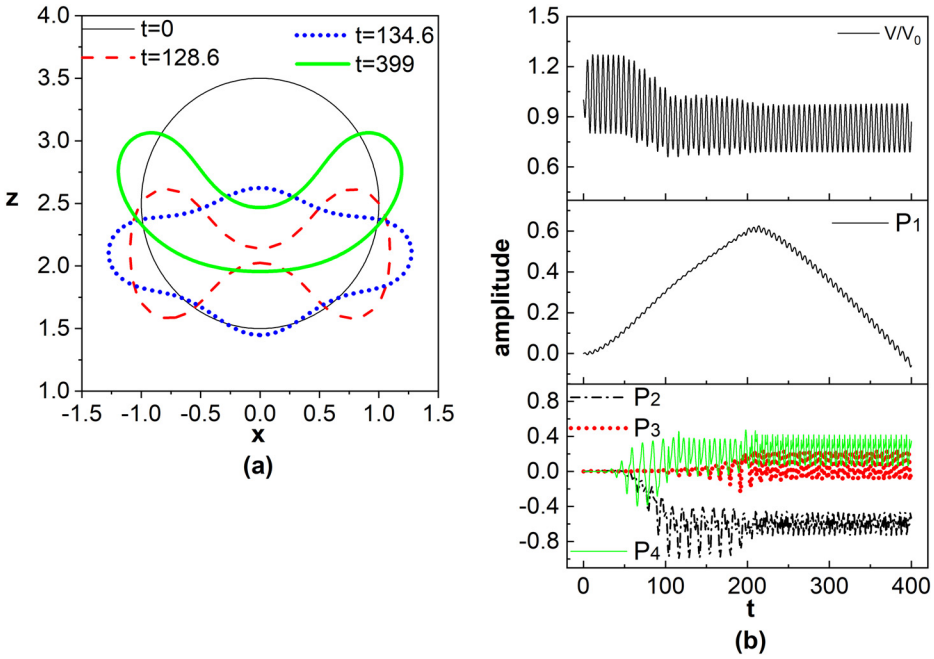

FIG. 6. (Color online) Temporal evolution of (a) bubble shape and (b) the volume, the translational mode P_1 and shape mode pulsation, for a lipid coated microbubble ($R_{SF} = 3.6\,\mu$m, $\mu_s = 60 \times 10^{-9}$ kg/s, $\chi = 0.24$ N/m, $k_B = 3 \times 10^{-14}$ N m, $\delta = 1$ nm) subject to an acoustic disturbance with $f = 1.7$ MHz and an initial prestress, $U_d = -0.46\,\mu$m when, $\mu_{sh}/\mu_s = 0.3$ and $\varepsilon = 0.7$, for a wall restricted flow with the initial distance from the wall set to $z_{c0} = 2.5$.

disturbances in the presence of a wall, pertains to their translational motion and their possible entrapment at the wall. As discussed in Vlachomitrou and Pelekasis (2021b), it is possible for contrast agents to get trapped at a small distance from the wall where they perform steady pulsations as long as the sound amplitude remains smaller than the critical threshold for parametric shape mode excitation. However, the latter study assumed equal values for the shear and dilatational shell viscosity and considered initially stress-free contrast agents. As will be demonstrated in the following discussion, the trapping procedure is indeed strongly affected by the onset of compression-only behavior. In fact, the shape acquired by the bubble as it oscillates may not only interrupt the trapping procedure but also reverse the translational motion with the microbubble gradually moving in the opposite direction. This is clearly demonstrated in Figs. 3–6, by inspecting the emerging shapes and the temporal evolution of the translational mode P_1 with its amplitude being associated with the instantaneous center of mass $z_c(t)$ via $a_{P_1}(t) = z_{c0} - z_c(t)$. The positive gradient of $a_{P_1}(t)$, averaged over a period of the pulsation until the onset of the steady compressed pulsations, denotes a translational motion towards the wall as a result of the secondary Bjerknes forces, in the manner described in Vlachomitrou and Pelekasis (2021a). It is clear from Figs. 3–6 that the translation of the bubble towards the wall continues even after the onset of the compression-only behavior as long as the shape of the bubble remains symmetric. In particular, as illustrated in Figs. 5(d) and 6(b), symmetric modes dominate when $40 < t < 100$ and $40 < t < 200$, respectively, and in this time interval the amplitude of P_1 increases with time. However, the motion of the bubble towards the wall is halted when the asymmetric mode P_3 develops, as the negative gradient of the translational mode P_1 indicates, with the bubble departure from the wall gradually increasing. Clearly then, the same transition from symmetric to asymmetric shapes as the bubble approaches the wall and its impact on the translational mode P_1 is expected to emerge in Fig. 4(c), albeit at a much later stage of the bubble motion in comparison with the time interval captured by the simulation in Fig. 4(c).

A different behavior is captured for a smaller discrepancy between the two shell viscosities as illustrated in Fig. 7. In particular, the parameter set employed in Figs. 7(a)–7(c) lies near the amplitude threshold of the envelope of the phase diagram that separates the compression-only region from trapped pulsations in Fig. 9(b). As a result, trapping occurs on the same time scale as parametric growth of shape modes and the bubble reaches the wall on a relatively short time interval, on the order of 100 periods of the forcing, since the increased sound amplitude ($\varepsilon = 1$) increases the translational velocity. The lubrication pressure in the region between the shell and the wall instigates shell buckling, generating the concave downward shapes. Due to the highly deformed and compressed shapes that the bubble acquires as it pulsates, Figs. 7(a) and 7(b), it exhibits compression-only behavior but eventually, $t \geq 190$, it is trapped near the wall where it performs steady pulsations as shown in Fig. 7(c). In this case, the shape around which the bubble oscillates is also asymmetric, but the marked difference with the cases shown in Figs. 3–6 is that the shape remains concave downwards which does not allow for an upward motion to develop, contrary to the concave up shapes obtained in Figs. 3, 5, and 6.

A more typical case of wall trapping is illustrated in Figs. 7(d)–7(f) for which compression-only behavior does not spontaneously emerge owing to the choice of viscoelastic shell parameters and sound amplitude; see also the relevant phase diagram provided in Fig. 9. Thus, the bubble is seen to constantly migrate towards the wall where it

https://doi.org/10.1121/10.0024007

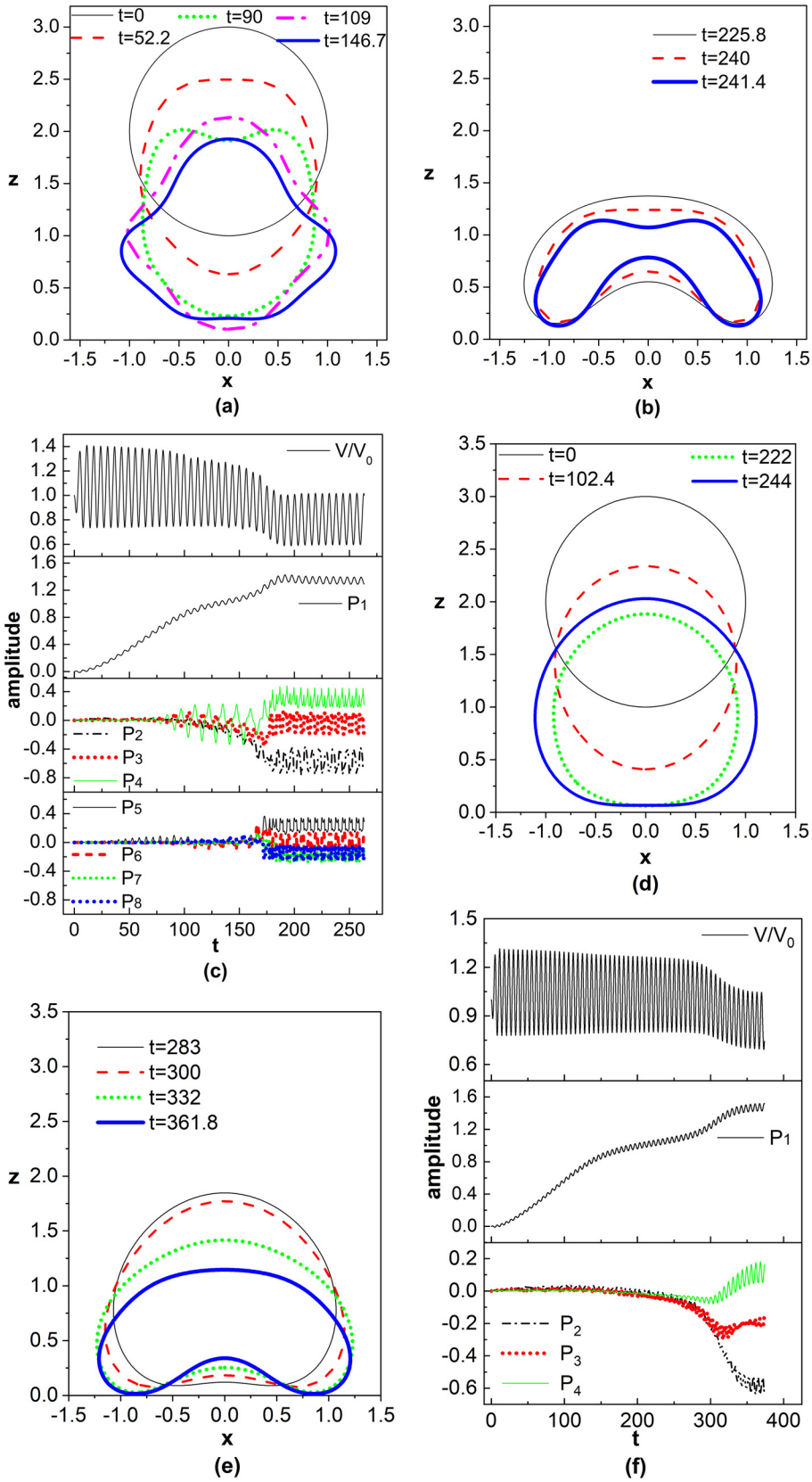

FIG. 7. (Color online) Temporal evolution of (a), (b), and (d) bubble shape as the bubble approaches the wall and during trapped pulsations, and (c) and (e) the volume, the translational mode P_1 and shape mode pulsation, for a lipid coated microbubble ($R_{SF} = 3.6\,\mu$m, $\mu_s = 60 \times 10^{-9}$ kg/s, $\chi = 0.24$ N/m, $k_B = 3 \times 10^{-14}$ N m, $\delta = 1$ nm) subject to an acoustic disturbance with $f = 1.7$ MHz, for an initial prestress $U_d = -0.46\,\mu$m, when the initial distance from the wall is set to $z_{c0} = 2$; (a), (b), and (c) $\varepsilon = 1$ and $\mu_{sh}/\mu_s = 0.5$, (d), (e), and (f) $\varepsilon = 0.8$ and $\mu_{sh}/\mu_s = 1$.

performs saturated pulsations with the nearly spherical shape reported by Vlachomitrou and Pelekasis (2021b). Furthermore, as can be gleaned upon inspection of Fig. 7(e), the time scale required for the bubble to reach the wall and commence trapped saturated pulsations is in accord with the predictions Vlachomitrou and Pelekasis (2021a,b), i.e., $t_{\text{trapping}} \sim O(1/\varepsilon)^2 z_{c0}{}^2$, in the context of secondary Bjerknes forces; see also Fig. 8(b) in Vlachomitrou and

Pelekasis (2021b). These predictions remain relevant to the extent that the bubble shape remains spherical, as will be the case despite the presence of prestress and the discrepancy between shear and dilatational viscosity, as long as compression-only behavior is not yet established. However, this will be the case, as can be gleaned from Fig. 7(e), which illustrates the gradual destabilization of the nearly spherical flattened shapes performing trapped pulsations in Fig. 7(d). This occurs in response to the lubrication pressure that develops in the region between the microbubble and the wall and instigates shell buckling, as expected for a sound amplitude above the static buckling threshold of the pre-stressed bubble interrogated in Figs. 7(d)–7(f); see also Figs. 2(b), 2(c), and 9(b) in the following. The microbubble thus exhibits concave downwards, significantly compressed buckled shapes around which it performs trapped pulsations, Fig. 7(f).

The pattern of asymmetric concave up shapes triggering translational motion away from the wall was a recurring theme in this study, as can be gleaned by cross-inspection of the time evolution of bubble shapes and the P_1 mode in Figs. 3–6. This is attributed to the balance between pressure and viscous forces on the microbubble surface. During the initial stages of the translational motion, the shape of the interface is nearly spherical and the secondary Bjerknes force pushes the bubble towards the wall with the viscous drag counterbalancing pressure drag, thus giving rise to a steady speed that increases quadratically with the sound amplitude ε; see also the analysis in Vlachomitrou and Pelekasis (2021a). Once compression-only behavior is established—characterized by oscillation around compressed and deformed buckled shapes—wall presence enhances the growth of asymmetric modes with P_3 being the dominant one. Typically, concave upward shapes arise signifying the increased pressure generated in the region between the protective shell and the wall. As a result, the force due to pressure drag is reversed acquiring a positive average value during a period of the forcing, pointing away from the wall. This pattern is clearly illustrated in Figs. 8(a) and 8(c) showing the time evolution of the mean forces due to pressure, $F_{P,av}$, and viscous dissipation, $F_{V,av}$, averaged over a period of the forcing, pertaining to simulations characterized by intense growth of the asymmetric P_3 mode. On the contrary when symmetric or concave downward shapes prevail, as is the case in Figs. 4 and 7, bubble-wall attraction persists due to the negative pressure drag, which points toward the wall until trapping takes place, see also Figs. 8(b) and 8(d). In all cases viscous dissipation counterbalances pressure, generating a nearly constant speed away from or towards the wall, depending on the bubble shape, with the former situation typically associated with the onset of compression-only response pattern characterized by pulsations around asymmetric concave up shapes. The latter situation arises for a sound amplitude at or below the threshold for parametric shape mode excitation, in which case the compression-only type response pattern emerges on the

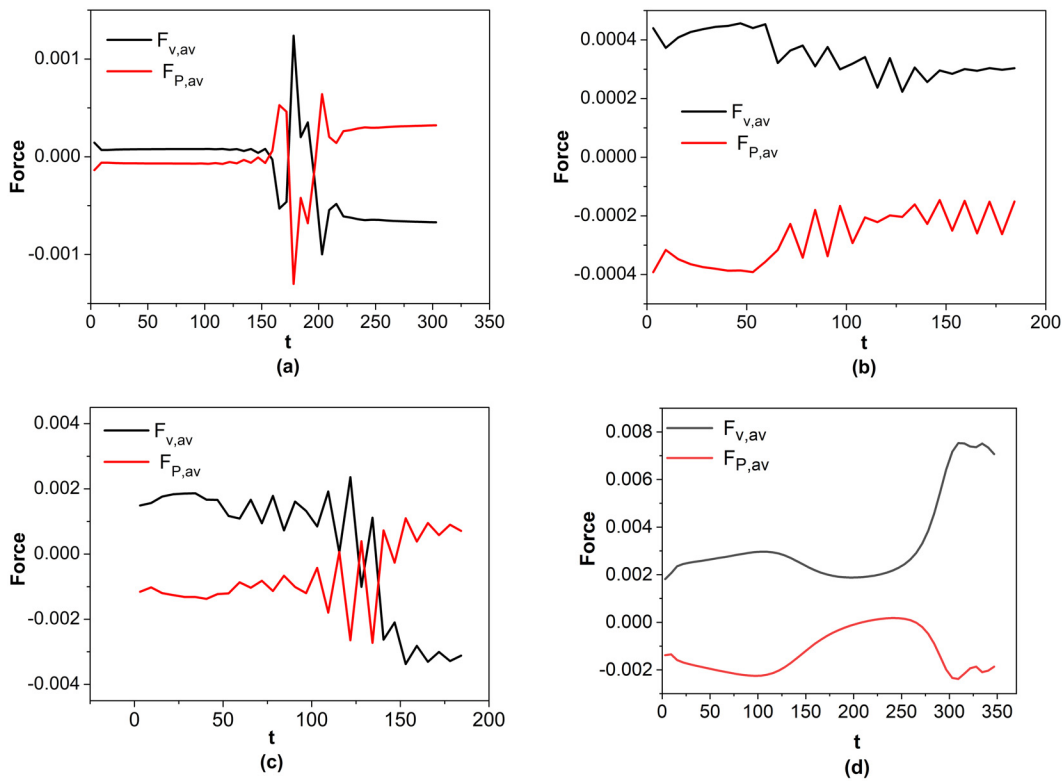

FIG. 8. (Color online) Time evolution of the mean force on the microbubble due to pressure, $F_{P,av}$, and viscous drag $F_{V,av}$, averaged over a period of the forcing, pertaining to the simulations presented in (a) Figs. 3(a) and 3(c), (b) Figs. 4(a) and 4(c), (c) Figs. 5(b) and 5(d), and (d) Figs. 7(d)–7(f).

https://doi.org/10.1121/10.0024007

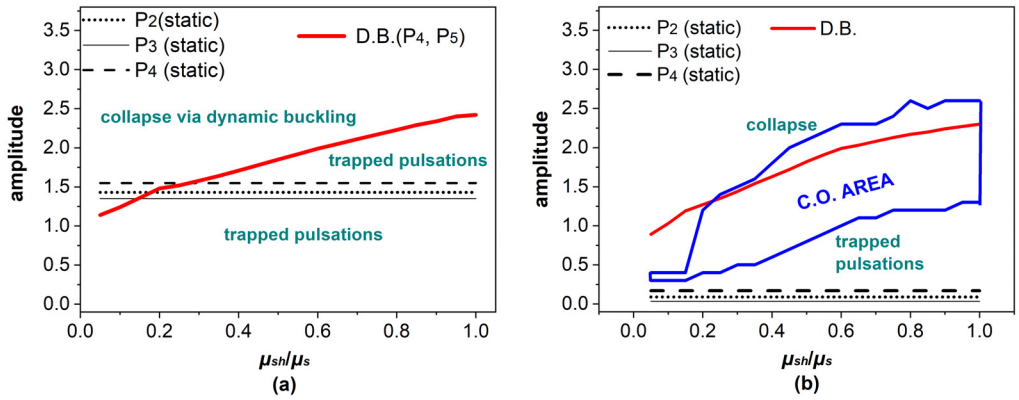

FIG. 9. (Color online) Mapping of the dynamic response of a contrast agent to an acoustic disturbance in a wall-bounded flow for (a) an initial stress-free state and (b) for an initially pre-stressed state of a lipid coated microbubble with increasing μ_{sh}/μ_s ratio subject to an acoustic frequency of $f = 1.7$ MHz, with ($z_{c0} = 4$) wall presence; $U_d = -0.46\,\mu$m; R_{SF}=3.6 μm, $\mu_s = 60 \times 10^{-9}$ kg/s, $\chi = 0.24$ N/m, $k_B = 3 \times 10^{-14}$ N m, $\delta = 1$ nm. The bounded area labeled "C.O. area" pertains to typical compression-only behavior obtained for sound amplitudes above the threshold for parametric shape mode excitation.

much longer time scale required for the nearly spherical trapped bubble to be destabilized and buckle, thus giving rise to the concave down shapes obtained in Fig. 7.

When wall presence is taken into account, an extensive parametric study was performed based on shell viscosity ratio and acoustic amplitude in order to construct phase diagrams describing the dynamic response pattern of coated microbubbles. Figure 9(a) typically summarizes the results obtained in Vlachomitrou and Pelekasis (2021b) for an initial stress-free state, enhanced with a parametric study based on the μ_{sh}/μ_s ratio. It is provided in order to facilitate comparison with cases examined in this paper for which prestress is present, also for fixed standoff distance $z_{c0} = 4$, as well as to summarize the complete behavior of coated microbubbles in the presence of a wall. The area identified as "C.O. area" in Fig. 9(b) was recovered when a certain amount of prestress was present, containing the region in the parameter space defined by the sound amplitude and shell viscosity ratio for which compression-only behavior was captured within 30 periods of the forcing. The simulations performed in the present study demonstrate that the mechanism identified in **I** for the onset of the compression-only behavior is not affected significantly by wall presence in the sense that it is still triggered by the same set of parameters as in the case of the unbounded flow, see "C.O. area" in Fig. 2(c). The latter region is very similar to the one identified as C.O. area for a dimensionless standoff distance $z_{c0} = 4$ in Fig. 9(b) since they are both associated with parametric shape mode excitation. For the same reason, simulations for different initial distances or larger time frame for the onset of compression-only behavior, reveal that the thresholds of the compression-only region are mildly affected. However, once we operate in the appropriate parameter range for shape mode excitation, as illustrated by the results presented in Figs. 3–7 pertaining to wall bounded flow, wall presence accelerates the onset of the phenomenon and alters the shape around which the bubble oscillates, favoring asymmetric shapes that are concave upwards. Furthermore, as can be gleaned upon comparing Figs. 9(a) and 9(b), when the compression-only behavior is triggered in the previous amplitude range entrapment of the bubble by the wall is often prevented due to the highly compressed and asymmetric deformed shapes that typically emerge. Asymmetric concave upward shapes reverse the bubble motion away from the wall, as illustrated in Figs. 3–6, due to the positive pressure drag as shown in Fig. 8, thus preventing trapping from taking place. For sound amplitudes that lie below the "C.O. area" in Fig. 9(c), the bubble performs nearly spherosymmetric pulsations as it moves towards the wall due to the secondary Bjerknes force. Then, the time that the bubble needs to reach the wall is not affected either by the initial prestress or the shear shell viscosity and it varies with the square of the standoff distance ($t \sim z_{c0}^2$) and the inverse of the square of the sound amplitude ($t \sim 1/\varepsilon^2$), exactly in the same manner identified in Vlachomitrou and Pelekasis (2021a,b). In the latter time frame, it is eventually trapped at the wall where it performs steady pulsations with nearly spherical flattened shapes; see also Figs. 7(d) and 7(f). However, on a longer time scale, the flattened shapes are destabilized, and significantly compressed concave down shapes emerge that also perform trapped saturated pulsations. Therefore, and provided enough time is available, below the amplitude threshold for parametric shape mode excitation the microbubble is trapped at the wall where it performs saturated compression-only pulsations that are characterized by concave down shapes.

V. CONCLUSIONS

We numerically investigate the impact of wall interaction on the onset of the compression-only behavior in the oscillations of a coated microbubble subject to acoustic disturbances. This is a continuation of a previous study by Pelekasis *et al.* (2022) that identified the mechanism that triggers the onset of the compression-only behavior which is associated with the onset of significantly compressed shapes that pulsate in the vicinity of static branches bifurcating from the spherosymmetric configuration. They showed that when the microbubble is initially pre-stressed, and

especially when the discrepancy between the two shell viscosities is large, the system dynamics lead toward pulsations around the static buckled shapes. In the present study, it is shown that this mechanism remains essentially unaffected by the wall presence or the initial distance from the wall in the sense that the wall only reduces the time required to trigger the effect as long as we remain within the parameter window for parametric shape mode excitation. However, it alters the compressed buckled shape around which the bubble oscillates as it usually favors asymmetry, especially as the distance from the wall is reduced.

We have also investigated the translational motion of contrast agents after the onset of the compression-only behavior to determine whether and how it affects the trapping procedure. In previous studies, Vlachomitrou and Pelekasis (2021a,b) considered initially stress-free contrast agents and identified the mechanism and the conditions that facilitate the trapping procedure when the two shell viscosities are equal. They found that for sound amplitudes smaller than the critical for dynamic buckling and loss of shell cohesion, the microbubble eventually gets trapped at a small distance from the wall where it performs saturated oscillations characterized by nearly spherical flattened shapes. In the present study, it is shown that above the amplitude threshold for parametric shape mode excitation, the compression-only behavior typically interrupts entrapment by favoring the onset of concave upward shapes and triggering migration in the opposite direction due to the positive pressure drag that develops. In fact, the direction of motion upon the onset of the compression-only behavior depends highly on the compressed buckled shape around which the bubble oscillates. Below the latter amplitude threshold and above the static buckling threshold, symmetric shapes or asymmetric shapes that are concave down emerge that continue to translate towards the wall due to the negative pressure drag. Eventually, saturated trapped pulsations are established and characterized initially by flattened nearly spherical shapes, but on a longer time scale by concave down shapes that exhibit the compression-only response pattern.

Carrying out an extensive parametric study, we have constructed phase diagrams (Fig. 9) that summarize the response of contrast agents to acoustic disturbances in the vicinity of a rigid wall. It is thus shown that when the bubble is initially pre-stressed the onset of compression-only behavior shrinks the region in phase space that allows for entrapment of the bubble at a nearby wall. This is an aspect of the response pattern that needs to be further investigated for varying wall properties as it impacts the potential of coated microbubbles to generate microstreaming patterns on the wall, thus facilitating novel drug delivery modalities, such as sonoporation, or even acoustic cleaning protocols.

ACKNOWLEDGMENTS

This research has been carried out within the framework of the invitation "Expression of interest for holders of doctoral diploma, for scholarship for postdoctoral research" of the University of Thessaly which is implemented by the University of Thessaly and is funded by the "Stavros Niarchos Foundation." Acknowledgment should also be given to the Greek Ministry of Education for financial support of this work through the project "ARISTEIA" in its early stages.

Barthes-Biesel, D., Diaz, A., and Dhenin, E. (**2002**). "Effect of constitutive laws for two-dimensional membranes on flow-induced capsule deformation," J. Fluid Mech. **460**, 211–222.
Church, C. C. (**1995**). "The effects of an elastic solid surface layer on the radial pulsations of gas bubbles," J. Acoust. Soc. Am. **97**(3), 1510–1521.
De Jong, N., Emmer, M., Chin, C. T., Bouakaz, A., Mastik, F., Lohse, D., and Versluis, M. (**2007**). "'Compression-only' behavior of phospholipid-coated contrast bubbles," Ultrasound Med. Biol. **33**(4), 653–656.
Dimakopoulos, Y., and Tsamopoulos, J. (**2003**). "A quasi-elliptic transformation for moving boundary problems with large anisotropic deformations," J. Comput. Phys. **192**(2), 494–522.
Doinikov, A. A., Haac, J. F., and Dayton, P. A. (**2009**). "Modeling of nonlinear viscous stress in encapsulating shells of lipid coated contrast agent microbubbles," Ultrasonics **49**(2), 269–275.
Katiyar, A., and Sarkar, K. (**2011**). "Excitation threshold for subharmonic generation from contrast microbubbles," J. Acoust. Soc. Am. **130**(5), 3137–3147
Khismatullin, D. B., and Nadim, A. (**2002**). "Radial oscillations of encapsulated microbubbles in viscoelastic liquids," Phys. Fluids **14**(10), 3534–3557.
Marmottant, P., and Hilgenfeldt, S. (**2003**). "Controlled vesicle deformation and lysis by single oscillating bubbles," Nature **423**, 153–156.
Marmottant, P., van der Meer, S., Emmer, M., Versluis, M., de Jong, N., Hilgenfeldt, S., and Lohse, D. (**2005**). "A model for large amplitude oscillations of coated bubbles accounting for buckling and rupture," J. Acoust. Soc. Am. **118**(6), 3499–3505.
Overlede, M. (**2009**). "Ultrasound contrast agents—Dynamics of coated microbubbles," Ph.D. thesis, University of Twente, Netherlands.
Paul, S., Katiyar, A., Sarkar, K., Chatterjee, D., Shi, W. T., and Forsberg, F. (**2010**). "Material characterization of the encapsulation of an ultrasound contrast microbubble and its subharmonic response: Strain-softening interfacial elasticity model," J. Acoust. Soc. Am. **127**(6), 3846–3857.
Pelekasis, N., Vlachomitrou, M., and Lytra, A. (**2022**). "Compression-only behavior: Effect of prestress and shell rheology on bifurcation diagrams and parametric stability of coated microbubbles in an unbounded flow," Phys. Rev. Fluids **7**, 113601.
Pozrikidis, C. (**2001**). "Effect of membrane bending stiffness on the deformation of capsules in simple shear flow," J. Fluid Mech. **440**, 269–291.
Sarkar, K., Shi, W. T., Chatterjee, D., and Forsberg, F. (**2005**). "Characterization of ultrasound contrast microbubbles using *in vitro* experiments and viscous and viscoelastic interface models for encapsulation," J. Acoust. Soc. Am. **118**(1), 539–550.
Shima, A., Tomita, Y., Gibson, D. C., and Blake, J. R. (**1989**). "The growth and collapse of cavitation bubbles near composite surfaces," J. Fluid Mech. **203**, 199–214.
Thomas, D. H., Looney, P., Steel, R., Pelekasis, N., McDicken, W. N., Anderson, T., and Sboros, V. (**2009**). "Acoustic detection of microbubble resonance," Appl. Phys. Lett. **94**(24), 243902.
Timoshenko, P., and Woinowsky-Krieger, S. (**1959**). *Theory of Plates and Shells* (McGraw-Hill, Singapore).
Tsiglifis, K., and Pelekasis, N. (**2008**). "Nonlinear radial oscillations of encapsulated microbubbles subject to ultrasound: The effect of membrane constitutive law," J. Acoust. Soc. Am. **123**(6), 4059–4070.
Tsiglifis, K., and Pelekasis, N. (**2011**). "Parametric stability and dynamic buckling of an encapsulated microbubble subject to acoustic disturbances," Phys. Fluids **23**, 012102.
Tsiveriotis, K., and Brown, R. A. (**1992**). "Boundary-conforming mapping applied to computations of highly deformed solidification interfaces," Numer. Methods Fluids **14**, 981–1003.
Vlachomitrou, M., and Pelekasis, N. (**2021a**). "Numerical study of the interaction between a pulsating coated microbubble and a rigid wall. I. Translational motion," Phys. Rev. Fluids **6**, 013601.
Vlachomitrou, M., and Pelekasis, N. (**2021b**). "Numerical study of the interaction between a pulsating coated microbubble and a rigid wall. II. Trapped pulsation," Phys. Rev. Fluids **6**, 013602.